Geophysical Journal International

Geophys. J. Int. (2010) **183,** 1501–1511 doi: 10.1111/j.1365-246X.2010.04806.x

An analytical approach for the scattering of SH waves by a symmetrical V-shaped canyon: deep case

Deng-How Tsaur, Kao-Hao Chang and Ming-Sheng Hsu

Department of Harbor and River Engineering, National Taiwan Ocean University, No. 2, Beining Rd., Jhongjheng Dist., Keelung City 202, Taiwan.
E-mail: hretdh@ntou.edu.tw

Accepted 2010 September 8. Received 2010 September 6; in original form 2010 July 17

SUMMARY

A novel analytical approach to the SH-waves scattering problem of a single deep symmetrical V-shaped canyon is presented. The adopted strategy of domain decomposition prevents the auxiliary boundary from being pierced by the lowest part of the canyon, and inherently encompasses the singular behaviour of the stress field around the bottom of the canyon. Appropriate wavefunctions and Graf's addition formulas are well utilized. The introduction of the method of images fulfills the stress-free condition at the ground level. In the deep V-shaped cases, comparisons with previously published data show good agreement. In the degenerate cases where the width of the canyon approaches zero, the presented results coincide with those obtained from the exact series solution of a single zero-thickness vertical edge crack. Both frequency- and time-domain results are given. Effects of the parameters on steady-state surface motions are illustrated and discussed. Transient changes in surface and subsurface displacement fields are included. The proposed series solution not only provides reliable results sufficiently under high-frequency excitations, but also fills the gap in the preceding cases of shallow canyons.

Key words: Earthquake ground motions; Theoretical seismology; Wave scattering and diffraction; Wave propagation.

1 INTRODUCTION

Surficial topography has been known for years as one of the leading factors affecting the characteristics of earthquake-induced ground motions. This is usually called as 'topographic effect'. Such term is closely related to the near-surface local geometrical properties, that is, the presence of canyons, hills, mountains, slopes, cliffs, etc. As a result, the sufficient evaluation on potential risks for the amplification of ground motions at a given site with discontinuities in elevation has been of great interests to researchers in seismology, geophysics, tectonics and natural hazards.

Canyons are one common type of natural landforms on the Earth's surface. The canyon shape depends on the characteristic of the current flowing through. In the mountainous region, steep gradient makes streams and rivers flow quickly downhill, and therefore rapid downcutting removes more sediments from the channel bottom than those from the sides. Such a geological process produces precipitous lateral walls and a narrow bottom, resembling the letter '*V*' in cross-section. Examples of V-shaped canyons are the Feitsui Canyon in Taiwan (see fig. 5 of Huang & Chiu 1995) and the San Fernando Valley in southern California (see fig. 2 of Boore 1973).

In a broad sense, simplified models may help one understand the phenomena of seismic wave propagation around real canyons. In fact, symmetrical V-shaped models have been one kind of most concerned geometries for fundamental studying. Since the early 1970s, a great deal of numerical approximate methods has been devised to cope with the problems of scattering and diffraction induced by a single symmetrical V-shaped canyon. Simply take the SH-waves cases for example: the Aki-Larner method (Bouchon 1973), the method of matched asymptotic expansions (Sabina & Willis 1975), the integral equation method (Sills 1978; Sánchez-Sesma & Rosenblueth 1979), the combined finite element and analytical technique (Shah *et al*. 1982), the hybrid method joining the finite and infinite elements together (Zhang & Zhao 1988), the complex function method (Liu & Han 1991), and the boundary element method (Hirai 1988; Takemiya & Fujiwara 1994) have been employed to solve related problems and to simulate possible ground surface motions. No doubt, most of the above approaches are more flexible for arbitrary terrains. However, the validity of their computed results must be tested strictly via exact solutions. It is well known that exact solutions derived by the method of separation of variables (MSV) are only limited to a few simple geometric shapes (e.g. Varadan *et al*. 1991). For a long time, since the V-shaped model does not belong to any separable coordinate system, the possibility of applying the MSV to such a case has been precluded, albeit a very simple case. Quite recently, Tsaur & Chang (2008) made a breakthrough

on the usage of the region-matching technique for the 'shallow' symmetrical V-shaped case. This promising technique not only defeated the intrinsic difficulty in utilizing the MSV, but also gave a rigorous series solution, which may be a best candidate for the exact solution.

As mentioned in the work of Tsaur & Chang (2008), the criterion of classification for the terms 'shallow' and 'deep' canyons is based on the depth-to-half-width ratio of the canyon. In doing the domain decomposition for the cases of 'shallow' canyons (whose depths are smaller than half-widths), the half-width of the canyon is taken as the radius of the semi-circular auxiliary boundary to enclose the whole canyon surface. Nevertheless, this trick does not work anymore for the cases of 'deep' canyons (whose depths are larger than half-widths) because the canyon bottom (i.e. the apex of the V) will pierce the auxiliary boundary. Thus, how to vanquish this predicament motivates this work.

In this paper, the authors come up with an ingenious strategy of domain decomposition to derive a series solution to the scattering problem induced by a single 'deep' symmetrical V-shaped canyon under plane SH-wave incidence. The proposed domain decomposition takes the canyon flanks as the radius of a circular-arc auxiliary boundary to encircle the faces of the canyon and to avoid the penetration in the auxiliary boundary. Incorporating the stress singularity condition (at the canyon bottom) into the wavefield expression of the enclosed subregion is the most pleasing trait in this adopted tactic. In addition, since the centre of the presented fictitious interface is below the ground level, the method of images is utilized to satisfy the requirement for zero stress normal to the horizontal ground surface.

Herein, the success of the solution procedure hinges on two key steps: (1) the appropriate selection of auxiliary boundaries and (2) the suitable usage of Graf's addition formulas. The first step decomposes the entire analysed region into several subregions, and facilitates the application of the MSV to every subregion. In other words, this step ensures that the construction of eigensolutions is well defined and well behaved in each individual subregion because those eigen-wavefields have automatically satisfied the governing Helmholtz equation and all boundary conditions except those on the auxiliary boundary. As to the second step, it accomplishes the necessary coordinate transformations.

The primary contributions of the present work are fourfold. First, the series solution proposed herein is novel since, to the authors' knowledge, the series solution to the problem under consideration is likely to be non-existent in the literature; moreover, it bridges the gap in the work of Tsaur & Chang (2008), which is only feasible for the cases of 'shallow' symmetrical V-shaped canyons. Second, the presented region-matching technique makes the usage of the MSV become possible for geometric shapes not fitting the corresponding coordinate systems. Three, the evaluation of steady-state responses up to a high-frequency range fulfils the calculation of transient responses easily. Four, the snapshots of time-domain underground motions enhance the understanding of this topic.

2 THEORETICAL FORMULATION

Consider a deep, symmetrical, V-shaped canyon embedded in a homogeneous, isotropic, linearly elastic half-plane (with shear modulus μ and shear wave velocity c_s). An infinite train of unit-amplitude plane SH waves (with angular frequency ω) is incident upon this canyon at an angle α to the y-axis. The geometric layout of the problem is illustrated in Fig. 1. The horizontal ground surface coincides

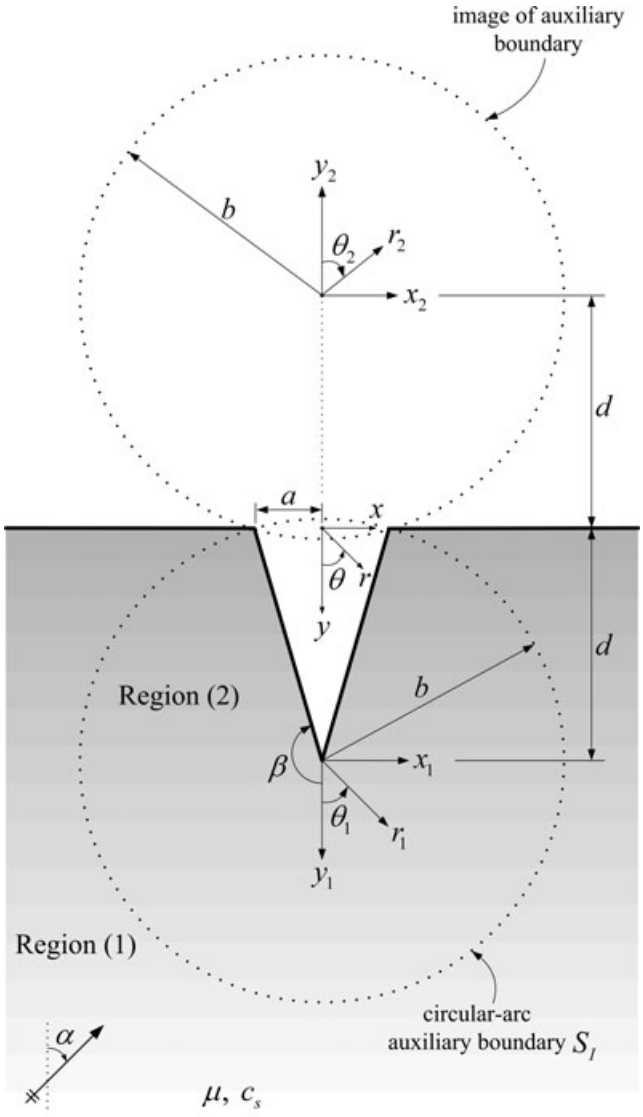

Figure 1. Geometric layout of the problem.

with the $y = 0$ plane. The canyon is supposed to be infinitely long along the z-direction, which is parallel to the canyon axis, so that the present problem is reduced to a 2-D form. The half-width and depth of the canyon is a and d, respectively. Both flanks of the canyon have the length of b. The angle measured from the positive y_1-axis to the canyon surface is β. The requirement for a 'deep' canyon studied herein is $a/d \leq 1$. Three Cartesian and three cylindrical coordinate systems will be employed; see Fig. 1. The origins of global coordinate systems (x, y) and (r, θ) are placed at the intersection of the horizontal ground surface and the symmetry axis of the canyon. The canyon bottom and its corresponding image point are, respectively, taken as the origins of two sets of local coordinate systems (i.e. (x_j, y_j) and (r_j, θ_j); $j = 1, 2$). For local coordinate systems (x_2, y_2) and (r_2, θ_2), the vertical axis is defined as positive going upwards, and the positive angle is measured clockwise from positive y_2-axis.

In order to enclose the canyon bottom completely, the canyon flank is taken as the radius of the circular-arc auxiliary boundary. As seen in Fig. 1, a circular-arc auxiliary boundary S_I (with radius b and central angle 2β) splits the half-plane into two regions, an open region (1) and an enclosed region (2). In these two regions,

the steady-state out-of-plane motions are required to satisfy the governing Helmholtz equations, namely

$$\nabla^2 u_j + k^2 u_j = 0, \quad j = 1, 2, \tag{1}$$

where ∇^2 is the cylindrical Laplacian, $k = \omega/c_s$ is the shear wavenumber and the subscripts, 1 and 2, designate the total displacement fields in regions (1) and (2), respectively. The harmonic time dependence is given by factor $\exp(\mathrm{i}\,\omega t)$ and suppressed throughout this paper.

In region (1), the zero-stress boundary conditions on the left- and right-hand horizontal ground surfaces are

$$\tau^{(1)}_{\theta z} = \frac{\mu}{r}\frac{\partial u_1}{\partial \theta}(r, \theta) = 0, \quad \text{for } r \geq a \quad \text{and} \quad \theta = \pm\frac{\pi}{2}. \tag{2}$$

In region (2), the traction-free boundary conditions on the canyon faces are

$$\tau^{(2)}_{\theta_1 z} = \frac{\mu}{r_1}\frac{\partial u_2}{\partial \theta_1}(r_1, \theta_1) = 0, \quad \text{for } r_1 < b \quad \text{and} \quad \theta_1 = \pm\beta. \tag{3}$$

On the auxiliary boundary S_I, two matching conditions, assuring the continuity of normal components of the displacement and stress fields between regions (1) and (2), are given by

$$u_1(r_1, \theta_1) = u_2(r_1, \theta_1), \quad \text{for } r_1 = b \quad \text{and} \quad |\theta_1| \leq \beta, \tag{4}$$

$$\tau^{(1)}_{r_1 z}(r_1, \theta_1) = \tau^{(2)}_{r_1 z}(r_1, \theta_1), \quad \text{for } r_1 = b \quad \text{and} \quad |\theta_1| \leq \beta. \tag{5}$$

For the problem under consideration, the application of the method of images is effective. By treating the horizontal ground surface as an ideal mirror, an image of the incident plane wave and an image of the fictitious interface S_I are both introduced. This step profits on the later construction of appropriate wavefunctions satisfying the boundary conditions on the horizontal ground surface. At present, the original problem to be solved is converted into an equivalent two-scatterer problem.

In open region (1), adding the incident and reflected fields together (the latter is a mirror image of the former), the free wavefield u^F in terms of the local coordinate system (r_1, θ_1) is of the form

$$\begin{aligned} u^F(r_1, \theta_1) = {} & \exp\left[\mathrm{i}kr_1\cos(\theta_1 + \alpha)\right] \\ & + \xi \cdot \exp\left[-\mathrm{i}kr_1\cos(\theta_1 - \alpha)\right], \end{aligned} \tag{6}$$

where $\xi = \exp(-2\mathrm{i}kd\cos\alpha)$ is the phase factor. Then, eq. (6) can be expanded as (see Watson 1958; Abramowitz & Stegun 1972)

$$\begin{aligned} u^F(r_1, \theta_1) = {} & \sum_{n=0}^{\infty} \varepsilon_n \left[i^n + \xi(-i)^n\right] J_n(kr_1)\cos n\alpha \cos n\theta_1 \\ & + \sum_{n=1}^{\infty} \varepsilon_n \left[-i^n + \xi(-i)^n\right] J_n(kr_1)\sin n\alpha \sin n\theta_1, \end{aligned} \tag{7}$$

where ε_n is the Neumann factor (which is equal to 1 if $n = 0$ and to 2 if $n \geq 1$) and $J_n(\cdot)$ denotes the nth order Bessel function of the first kind.

When the incident wave and its mirror reflection impinge, respectively, upon the auxiliary boundary S_I and its image, two scattered waves generate. The resultant scattered field u^S is the sum of the two scattering components propagating radially outward from the canyon bottom and its image, respectively. The proper wavefunction of u^S, satisfying the Helmholtz equation (eq. 1) and Sommerfeld radiation condition at infinity, can be written as

$$\begin{aligned} u^S = {} & \sum_{n=0}^{\infty} A_n \left[H_n^{(2)}(kr_1)\cos n\theta_1 + H_n^{(2)}(kr_2)\cos n\theta_2\right] \\ & + \sum_{n=1}^{\infty} B_n \left[H_n^{(2)}(kr_1)\sin n\theta_1 + H_n^{(2)}(kr_2)\sin n\theta_2\right], \end{aligned} \tag{8}$$

where $H_n^{(2)}(\cdot)$ are the nth order Hankel functions of the second kind, and the complex expansion coefficients A_n and B_n are unknown.

As can be seen in eqs (7) and (8), the zero-stress condition on the horizontal ground surface (eq. 2) is satisfied automatically as a natural consequence of the symmetry of the equivalent two-object scattering system.

The union of the free wavefield u^F and the resultant scattered wavefield u^S gives the total wavefield u_1 in region (1), that is,

$$u_1 = u^F + u^S. \tag{9}$$

In enclosed region (2), the wavefield u_2, satisfying the Helmholtz equation (eq. 1) and the traction-free boundary conditions on canyon surfaces (eq. 3), can be expressed as

$$\begin{aligned} u_2(r_1, \theta_1) = {} & \sum_{n=0}^{\infty} C_n J_{2n\nu}(kr_1)\cos(2n)\nu\theta_1 \\ & + \sum_{n=0}^{\infty} D_n J_{(2n+1)\nu}(kr_1)\sin(2n+1)\nu\theta_1 \end{aligned} \tag{10}$$

in which $\nu = \pi/(2\beta)$ and the coefficients C_n and D_n are to be determined. Notice that eq. (10) suffices the requirement for the stress singularity existing near the canyon bottom. This feature underlines the fact that the wavefield solution in region (2) is well behaved everywhere.

Next, in order to match the boundary conditions across the auxiliary interface between regions (1) and (2), the required coordinate translations for Hankel functions are carried out via the Graf's addition formula (see Watson 1958), which are rewritten in a suitable form for our purpose, that is,

$$\begin{aligned} & H_n^{(2)}(kr_2)\begin{Bmatrix}\cos n\theta_2 \\ \sin n\theta_2\end{Bmatrix} \\ & = \sum_{m=0}^{\infty}(-1)^m J_m(kr_1)\begin{Bmatrix}U^+_{m,n}(2kd)\cos m\theta_1 \\ U^-_{m,n}(2kd)\sin m\theta_1\end{Bmatrix} \end{aligned} \tag{11}$$

in which

$$U^{\pm}_{m,n}(\cdot) = \frac{\varepsilon_m}{2}\left[(-1)^n H^{(2)}_{m+n}(\cdot) \pm H^{(2)}_{m-n}(\cdot)\right]. \tag{12}$$

Concerning the scattered wave generated from the image of the auxiliary boundary S_I, making use of eq. (11) shifts its coordinate system from (r_2, θ_2) to (r_1, θ_1). So, the total scattered wavefield u^S given in eq. (8) is re-expressed as

$$\begin{aligned} u^S(r_1, \theta_1) = {} & \sum_{n=0}^{\infty} A_n \left[H_n^{(2)}(kr_1)\cos n\theta_1 \right. \\ & \left. + \sum_{m=0}^{\infty}(-1)^m J_m(kr_1)U^+_{m,n}(2kd)\cos m\theta_1\right] \\ & + \sum_{n=1}^{\infty} B_n \left[H_n^{(2)}(kr_1)\sin n\theta_1 \right. \\ & \left. + \sum_{m=0}^{\infty}(-1)^m J_m(kr_1)U^-_{m,n}(2kd)\sin m\theta_1\right]. \end{aligned} \tag{13}$$

Multiplying the matching conditions (eqs 4 and 5) by cosine functions, integrating over the range $[-\beta, \beta]$, re-arranging, and truncating the infinite series to a finite number of terms yield the following coupled systems of linear algebraic equations,

$$\sum_{n=0}^{N-1} A_n \left[H_n^{(2)}(kb) I_{n,q}^{C1}(\beta) + \sum_{m=0}^{M-1} (-1)^m J_m(kb) U_{m,n}^{+}(2kd) I_{m,q}^{C1}(\beta) \right] - \sum_{n=0}^{N-1} C_n J_{2n\nu}(kb) I_{2n,q}^{C2}(\beta) = -\sum_{n=0}^{N-1} \varepsilon_n \left[i^n + \xi(-i)^n \right] J_n(kb) I_{n,q}^{C1}(\beta) \cos n\alpha, \quad q = 0, 1, 2, \cdots, N-1 \tag{14}$$

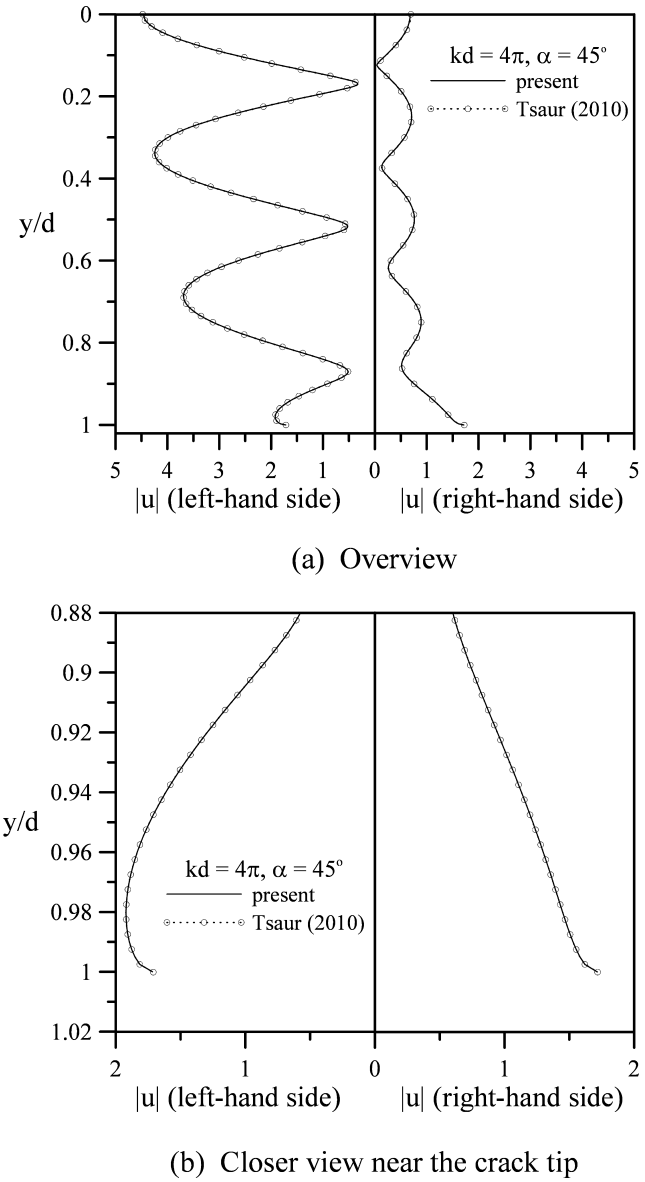

Figure 2. Displacement amplitudes on the crack face for comparison with the exact solution of Tsaur (2010).

$$\sum_{n=0}^{N-1} A_n \left[H_n^{(2)'}(kb) I_{2q,n}^{C2}(\beta) + \sum_{m=0}^{M-1} (-1)^m J_m'(kb) U_{m,n}^{+}(2kd) I_{2q,m}^{C2}(\beta) \right] - C_q J_{2q\nu}'(kb) \left[\frac{2\beta}{\varepsilon_q} + \frac{\sin(4q\beta\nu)}{4q\nu - \varepsilon_q + 2} \right] = -\sum_{n=0}^{N-1} \varepsilon_n \left[i^n + \xi(-i)^n \right] J_n'(kb) I_{2q,n}^{C2}(\beta) \cos n\alpha, \quad q = 0, 1, 2, \cdots, N-1, \tag{15}$$

where the expressions of $I_{n,q}^{C1}(\beta)$ and $I_{n,q}^{C2}(\beta)$ are given in Appendix A (see eqs A1 and A2), and the prime notation means differentiation with respect to the argument. The summation indexes n and m are, respectively, truncated to $N-1$ and $M-1$ terms, while the indexes q are selected to be $N-1$. Apparently, eqs (14) and (15) constitute a system of $2N$ equations with $2N$ unknowns. Expansion coefficients A_n and C_n can be solved simultaneously by standard matrix techniques.

Similarly, multiplying the continuity conditions (eqs 4 and 5) by sine functions, integrating over the range $[-\beta, \beta]$, rearranging, and truncating the infinite series result in another coupled systems of $2N$ equations for the unknown coefficients B_n and D_n,

$$\sum_{n=1}^{N} B_n \left[H_n^{(2)}(kb) I_{n,q}^{S1}(\beta) + \sum_{m=1}^{M} (-1)^m J_m(kb) U_{m,n}^{-}(2kd) I_{m,q}^{S1}(\beta) \right] - \sum_{n=0}^{N-1} D_n J_{(2n+1)\nu}(kb) I_{2n+1,q}^{S2}(\beta) = -\sum_{n=1}^{N} \varepsilon_n \left[-i^n + \xi(-i)^n \right] J_n(kb) I_{n,q}^{S1}(\beta) \sin n\alpha, \quad q = 1, 2, 3, \cdots, N \tag{16}$$

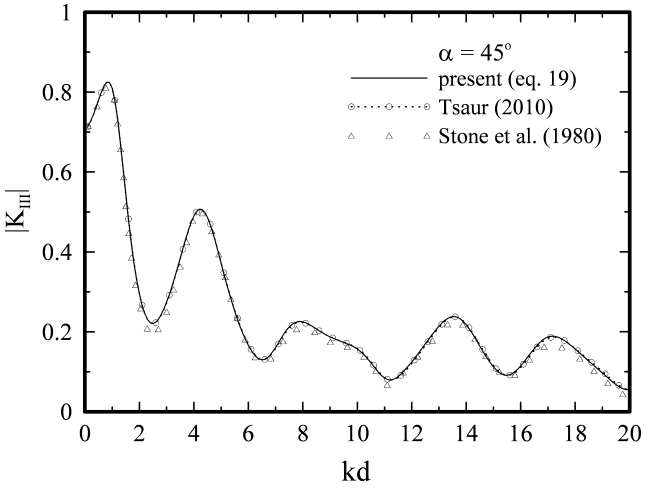

Figure 3. Dimensionless DSIF versus kd for comparison with the results of Tsaur (2010) and Stone *et al.* (1980).

$$\sum_{n=1}^{N} B_n \Bigg[H_n^{(2)'}(kb) I_{2q+1,n}^{S2}(\beta) + \sum_{m=1}^{M} (-1)^m J'_m(kb) U^{-}_{m,n}(2kd) I_{2q+1,m}^{S2}(\beta) \Bigg] - D_q J'_{(2q+1)\nu}(kb) \left\{ \beta - \frac{\sin[2(2q+1)\beta\nu]}{2(2q+1)\nu} \right\} = -\sum_{n=1}^{N} \varepsilon_n [-i^n + \xi(-i)^n] J'_n(kb) I_{2q+1,n}^{S2}(\beta) \sin n\alpha, \quad q = 0, 1, 2, \cdots, N-1, \tag{17}$$

where the expressions of $I_{n,q}^{S1}(\beta)$ and $I_{n,q}^{S2}(\beta)$ are given in Appendix A (see eqs A3 and A4).

When $\beta = \pi$, the V-shaped case will turn into the case of a vertical edge crack with length d and zero thickness. For such a limiting case, the authors' computed results coincide with those of existing works. Detailed comparisons will be shown in Section 3.

For a specified location in the corresponding region, the displacement amplitude $|u|$ is calculated from the expressions of wavefields (see eqs 9 and 10), that is,

$$|u| = \begin{cases} |u_1| = \sqrt{[\mathrm{Re}(u_1)]^2 + [\mathrm{Im}(u_1)]^2}, & \text{for region (1)} \\ |u_2| = \sqrt{[\mathrm{Re}(u_2)]^2 + [\mathrm{Im}(u_2)]^2}, & \text{for region (2),} \end{cases} \tag{18}$$

where $\mathrm{Re}(\cdot)$ and $\mathrm{Im}(\cdot)$ are, respectively, the real and imaginary part of a complex expression. Notice that in Section 3, the free wavefield u^F is directly evaluated by eq. (6) when computing the total displacement amplitude in region (1).

3 NUMERICAL RESULTS AND DISCUSSIONS

3.1 Frequency-domain responses

Convergence tests are carried out first to determine the truncation values (i.e. N and M) of the infinite series in eqs (14)–(17). It is worth emphasizing that the M terms of summation should be accurately computed by numerically testing for their convergence, thereby leaving only one parameter (i.e. N terms of summation) to eliminate the phenomenon of relative convergence. Based on a sequence of numerical experiments, $M = 200$ terms are adequate to plot all charts hereafter. Generally, more terms of N are required as

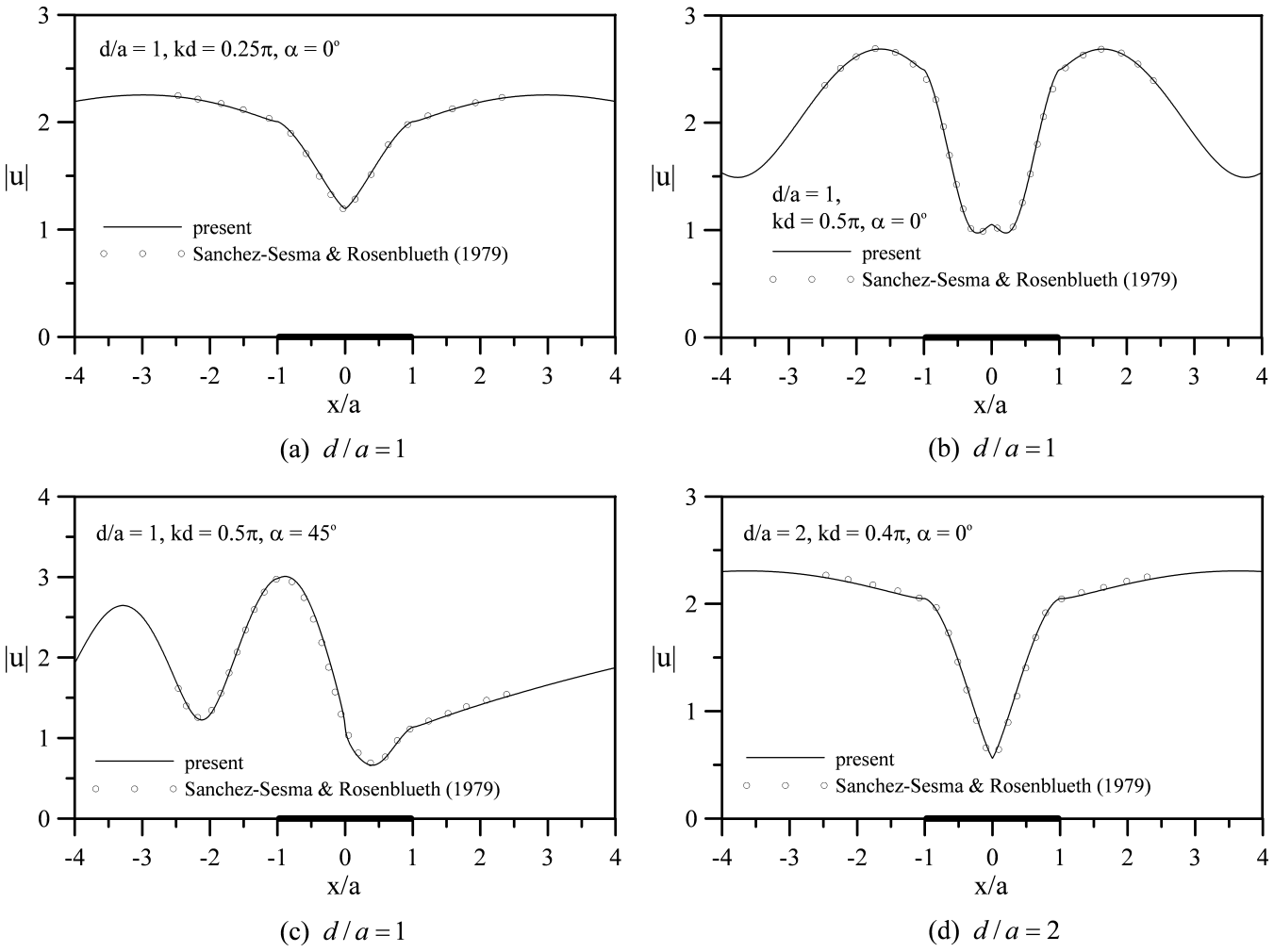

Figure 4. Surface motions versus x/a for comparison with the results of Sánchez-Sesma & Rosenblueth (1979).

the dimensionless wavenumber kd increases. For example, the convergence is achieved at $N = 22$ for $kd = 3\pi$ and at $N = 46$ for $kd = 10\pi$. For a relatively high value of $kd = 50\pi$, $N = 178$ is sufficient. This clearly shows that the derived series solution is still efficient in much higher frequency range. Even though the canyon bottom is a stress singular point, the convergence of displacement amplitudes is good. This is as expected since the present solution naturally incorporates the stress singularity into the eigen-expression of region (2) (see eq. 10).

3.1.1 Validation for the limiting case

A limiting case exists as the width of the canyon approaches zero. In this circumstance, the V-shaped case changes into the crack case with infinitesimal thickness. Since recently Tsaur (2010) has derived an exact series solution to the scattering and diffraction problems of a vertical edge crack under antiplane shear wave incidence, the cases for displacement amplitudes on the crack faces shown in his figs 3(b), 4(b), 5(b) and 6(b) are taken as validation examples. For brevity, only the case at $kd = 4\pi$ and $\alpha = 45^\circ$ is illustrated in Fig. 2. The plotted range of the dimensionless vertical distance is from the crack mouth ($y/d = 0$) to the crack tip ($y/d = 1$). As seen in Fig. 2(a), the present results are in good agreement with those of Tsaur (2010). Even take closer looks at the crack tip, both results match quite well with each other (see Fig. 2b).

In order to exhibit the better performance of derived series solution on the behaviour of singular stress field in the vicinity of the crack tip, the dimensionless dynamic stress intensity factor (DSIF) K_{III} is approximately computed through the crack opening displacement (COD). A simple formula given by Datta & Shah (1982) is adopted and rewritten, that is,

$$K_{\mathrm{III}} = \frac{1}{4k\sqrt{2dh}}\left[4(u_6 - u_4) - (u_3 - u_2)\right], \tag{19}$$

where h is the distance measured from the crack tip, and the subscripts (2, 3, 4 and 6) denote the displacements on the crack faces at specified positions (see fig. 2 of Tsaur 2010). Here, the suggested value of h/d is 0.01.

Fig. 3 displays the dimensionless DSIF against the frequency kd at $\alpha = 45^\circ$. As observed in Fig. 3, the results obtained by eq. (19) coincide with those shown in fig. 8(b) of Tsaur (2010) and

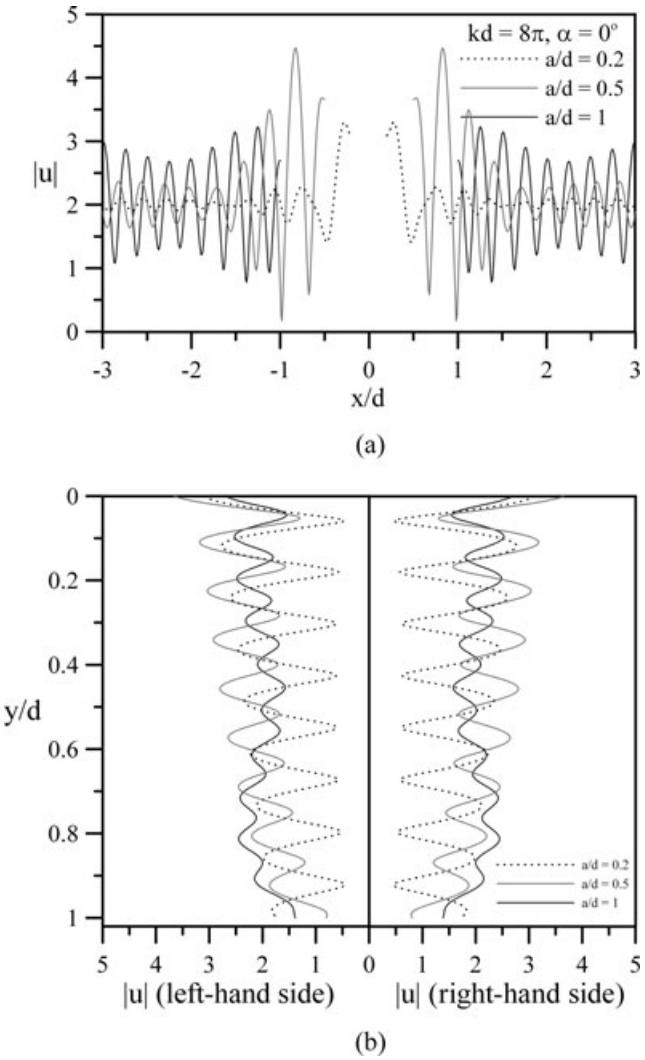

Figure 5. Surface motions versus x/d and y/d at $kd = 8\pi$ and $\alpha = 0^\circ$. (a) Motions on the horizontal ground surface, (b) motions on the canyon surface.

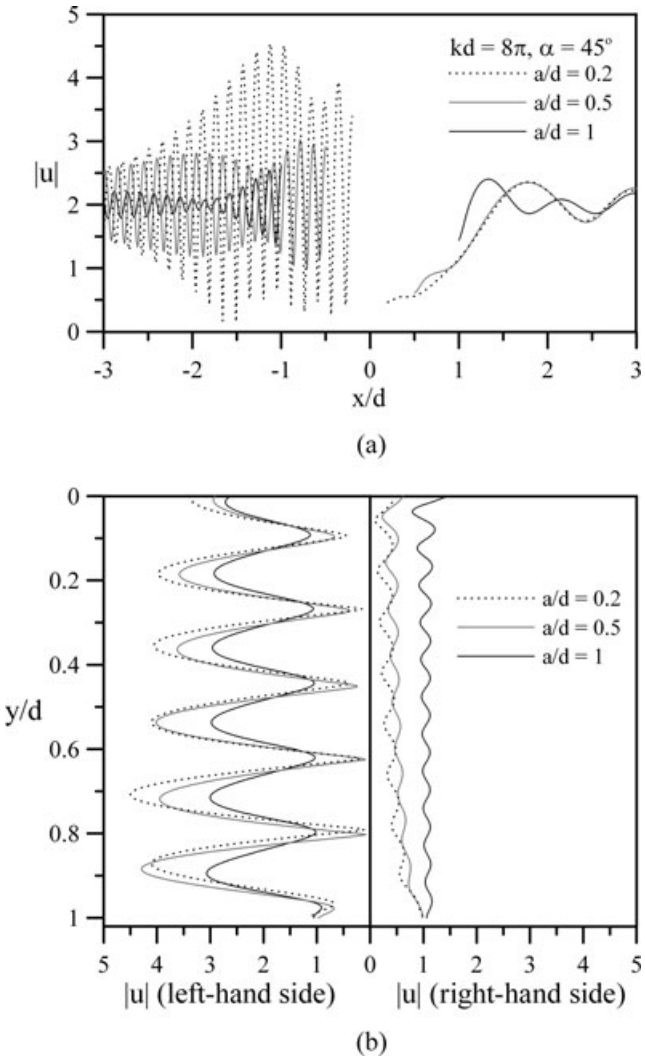

Figure 6. Surface motions versus x/d and y/d at $kd = 8\pi$ and $\alpha = 45^\circ$. (a) Motions on the horizontal ground surface, (b) motions on the canyon surface.

in fig. 3 of Stone *et al.* (1980). The credit for these good results of extremely near-field stress goes to the inclusion of the near-tip stress singularity in the present derived series solution.

3.1.2 Validation for the deep V-shaped case

In order to confirm the correctness of series formulations derived in eqs (14)–(17) for deep V-shaped cases, the displacement amplitudes on the horizontal ground surface and canyon surface shown in figs 5, 6 and 9 of Sánchez-Sesma & Rosenblueth (1979) are calculated in Fig. 4. Figs 4(a) and (b) are for $d/a = 1$ at vertical incidence ($\alpha = 0^\circ$) with $kd = 0.25\pi$ and 0.5π, respectively. Fig. 4(c) is for $d/a = 1$ at oblique incidence ($\alpha = 45^\circ$) with $kd = 0.5\pi$. Fig. 4(d) is for $d/a = 2$ at vertical incidence ($\alpha = 0^\circ$) with $kd = 0.4\pi$. The plotted range of the dimensionless horizontal distance is from $x/a = -4$ to 4. The corresponding position of the canyon surface is within the range from $x/a = -1$ to 1 (bold line). From Fig. 4, one can find that comparisons between our results and those of Sánchez-Sesma & Rosenblueth (1979) are good. This ensures that there are no mistakes in deriving eqs (14)–(17).

3.1.3 Surface motion for different parameters

In order to demonstrate the effect of the steepness of canyon sides on the displacement amplitude $|u|$, the surface responses for $a/d = 0.2$, 0.5 and 1 at $kd = 8\pi$ are calculated. Figs 5 and 6 are, respectively, the vertically and obliquely incident cases (i.e. $\alpha = 0^\circ$ and 45°). The case of $a/d = 1$ corresponds to that of an isosceles right-angled triangular canyon. Also, note that the V-shaped canyon is steeper when the value of a/d is smaller. In addition, Figs 7 and 8 further display the variations in surface ground motion as the steepness of canyon sides changes. The former is for vertical incidence ($\alpha = 0^\circ$), while the latter is for oblique incidence ($\alpha = 45^\circ$).

As seen in Figs 5 and 7, the displacement amplitudes under vertical incidence ($\alpha = 0^\circ$) are symmetrical about the y-axis due to the canyon symmetry. In the range of about $0.1 \le a/d \le 0.5$, one can find that the maximum response amplitude mainly occurs near the intersection of the horizontal ground surface and canyon surface. This may imply that there is a phenomenon of wave focusing. In Fig. 7(a), the amplified region becomes wider in the range of about $0.6 \le a/d \le 0.9$. Besides, when the value of a/d goes from 1 to 0 (meaning that the canyon gets steeper), the response of horizontal ground surface tends to be equal to 2 (see Figs 5a and 7a). This

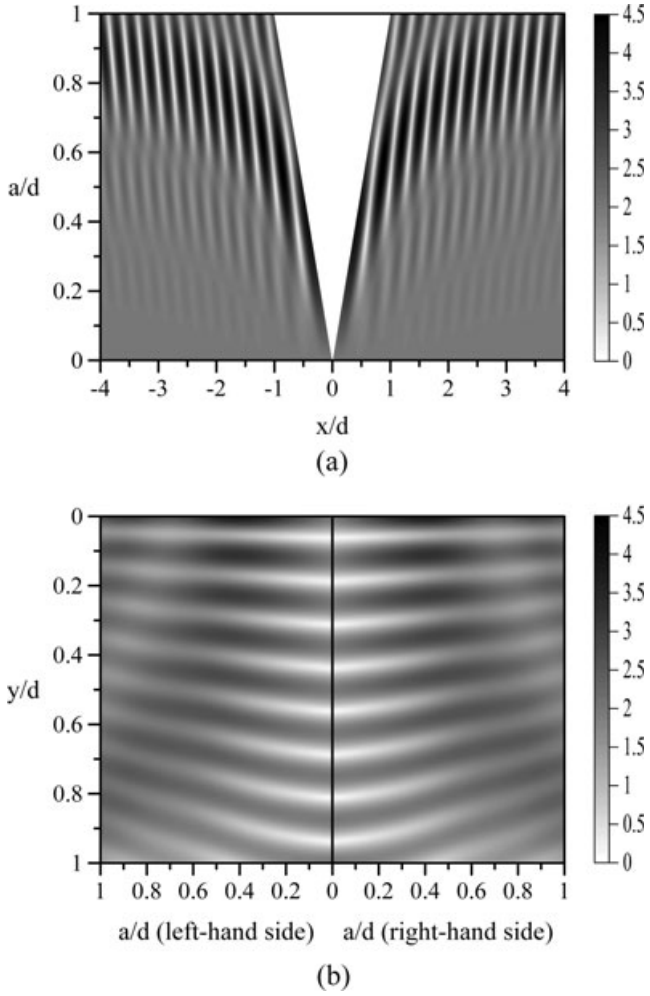

Figure 7. Surface displacements against a/d at $kd = 8\pi$ and $\alpha = 0^\circ$. (a) Displacements on the horizontal ground surface, (b) displacements on the canyon surface.

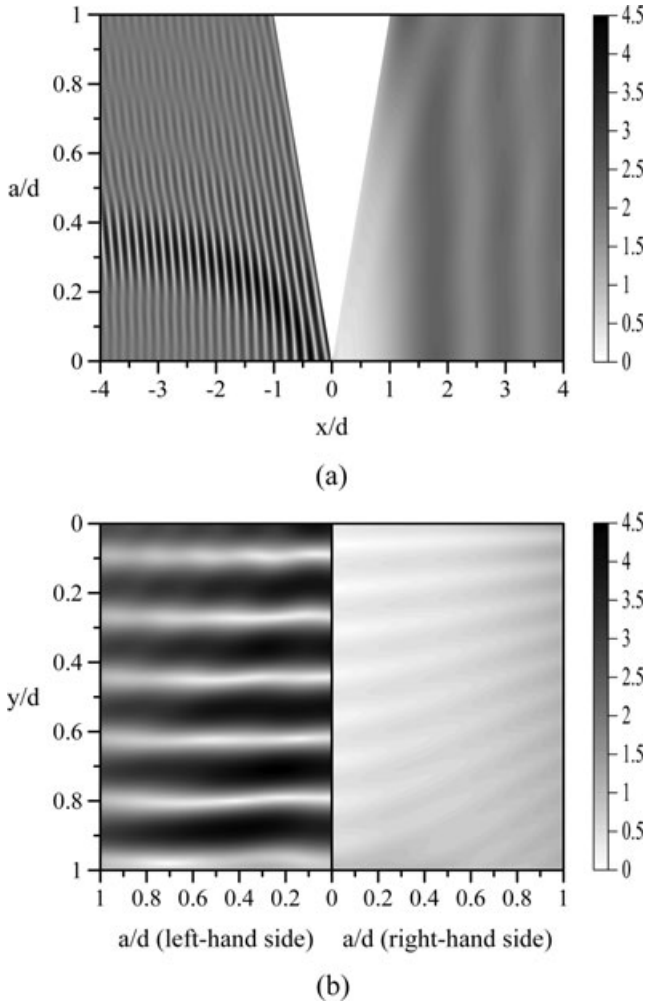

Figure 8. Surface displacements against a/d at $kd = 8\pi$ and $\alpha = 45^\circ$. (a) Displacements on the horizontal ground surface, (b) displacements on the canyon surface.

is because the vertical incident wave cannot feel the null-thickness canyon anymore so that no scattered waves are generated.

In Figs 6(a) and 8(a), motions on the left-hand horizontal ground surface seem to be sensitive to the change in canyon steepness, especially for those varying intensely in the region of $0.25 \leq a/d \leq 0.4$. On the right-hand horizontal ground surface, the displacement amplitudes change gradually due to the shielding effect provided by the canyon. As it is observed from Fig. 6(a), the maximum peak value for $a/d = 0.5$ reaches about 3, while that for $a/d = 0.2$ exceeds 4. From Figs 6(b) and 8(b), the values of surface amplitudes on the illuminated side are, for the most part, higher than those on the shaded side. On the left-hand canyon face, the oscillatory trend of ground motions is similar (i.e. the peak and dip values occur at nearly the same places). Furthermore, the largest amplification values for the cases of $0.8 \leq a/d \leq 1$ are about 1.5, while those for $0 \leq a/d \leq 0.5$ can be greater than 2. On the right-hand canyon face, the de-amplification behaviour of the ground shaking gets stronger when the canyon becomes steeper.

For the shake of revealing the influence of the dimensionless frequency on surface motions, Figs 9 and 10 gives the spectral variation in displacement amplitudes for $a/d = 0.25$ at vertical and oblique incidence ($\alpha = 0^\circ$ and 45°), respectively. In Fig. 9, the symmetrical patterns can be observed, as expected under symmetrical excitation.

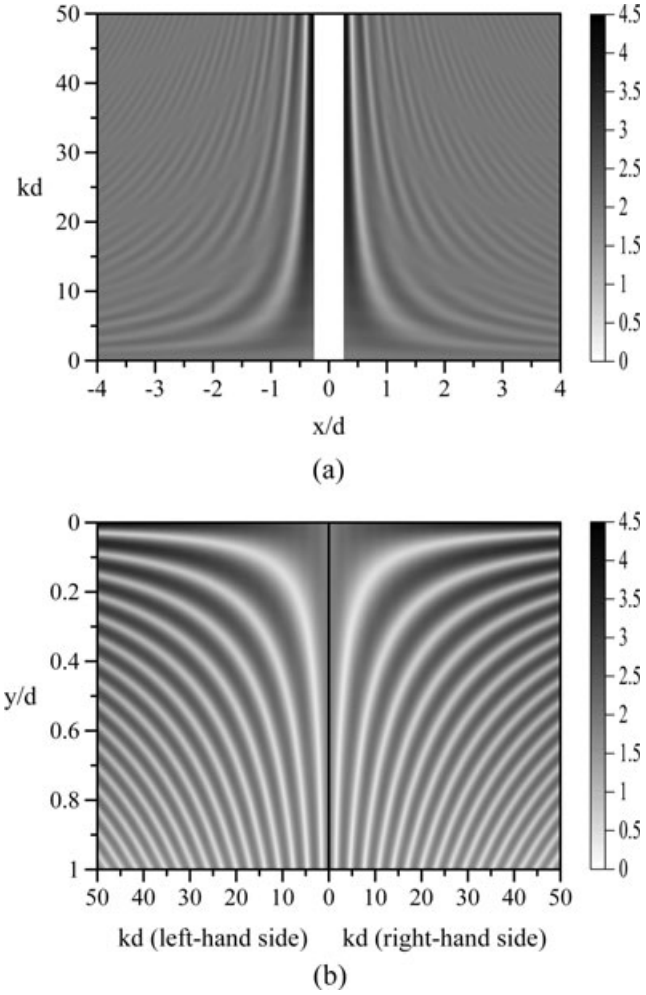

Figure 9. Spectral variation in surface displacements for $a/d = 0.25$ at $\alpha = 0^\circ$. (a) Displacements on the horizontal ground surface, (b) displacements on the canyon surface.

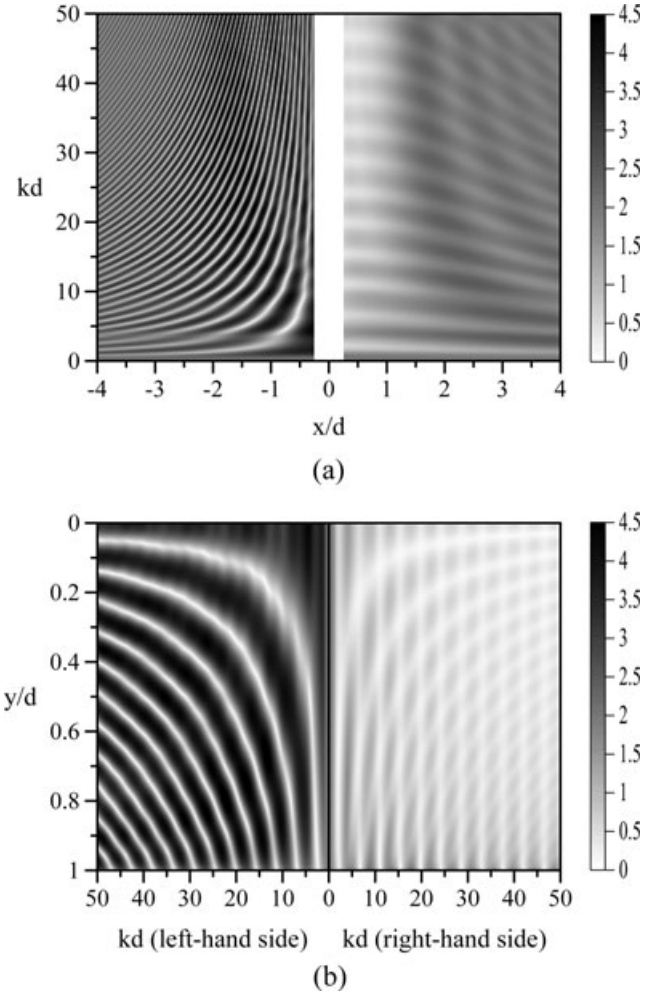

Figure 10. Spectral variation in surface displacements for $a/d = 0.25$ at $\alpha = 45^\circ$. (a) Displacements on the horizontal ground surface, (b) displacements on the canyon surface.

Also, the concentration of wave energy can be found near the left and right upper corners of the canyon (whose locations are at $x/d = \pm 0.25$ in Fig. 9(a) and $y/d = 0$ in Fig. 9b), especially for the cases of high-frequency incident waves. From Fig. 10, one can see that the difference in surface motions between illuminated and shaded zones is conspicuous. The surface motions to the left of the canyon are more complex and oscillatory than those to the right.

3.2 Time-domain responses

In this subsection, the model response in the time domain is easily obtained from the frequency-domain solutions using the fast Fourier transform algorithm. The incident signal, a symmetric Ricker wavelet (e.g. Kawase 1988), is defined as

$$u(t) = \left(2\pi^2 f_c^2 t^2 - 1\right) \exp\left(-\pi^2 f_c^2 t^2\right), \tag{20}$$

where f_c is the characteristic frequency of a wavelet, which is selected here to be 1.5 Hz. The calculated frequencies are 96 in total, ranging from 0 to 6 Hz with an interval of 0.0625 Hz. The time window is chosen as 16 s. The canyon depth d and shear wave velocity of the half-space c_s are, respectively, set to be 1 km and 1 km s^{-1}. The reference point taken for $t = 0$ s is specified at the position (0, 4) for vertical incidence and at (−4, 0) for grazing incidence.

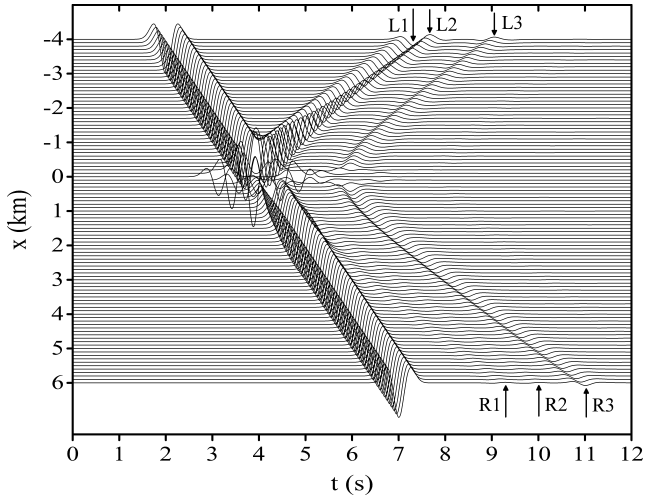

Figure 11. Synthetic seismogram for $a/d = 0.25$ at $\alpha = 30^\circ$.

In order to obtain a clear idea of transient motions on the horizontal ground surface and canyon surface, a synthetic seismogram under oblique incidence ($\alpha = 30^\circ$) is plotted in Fig. 11, which contains 101 time series received from equally spaced stations located along the horizontal ground surface between $x = -4$ and 6 km. Furthermore, 12 snapshots for the transient variation in underground motion at oblique incidence ($\alpha = 30^\circ$) are illustrated in Fig. 12. In each frame, the computational region within the rectangle of $[-4, 4] \times [0, 4]$ is discretized into 320×160 meshes with uniform spacing. For discriminating the patterns of scattered wavefields easily, the greyscale values are set to range between -0.2 and 0.2.

From Fig. 11, one can find that at stations near the left- and right-hand upper corners of the canyon ($x = \pm 0.25$ km), there has been a substantial change in the recorded waveforms at about $t = 4.0$ s. At this moment, the surface motion near the left-hand upper corner (LUC) of the canyon is amplified due to the constructive interference between the reflected wave from the horizontal ground surface and scattered wave from the LUC of the canyon. Near the right-hand upper corner (RUC) of the canyon, the surface motion is

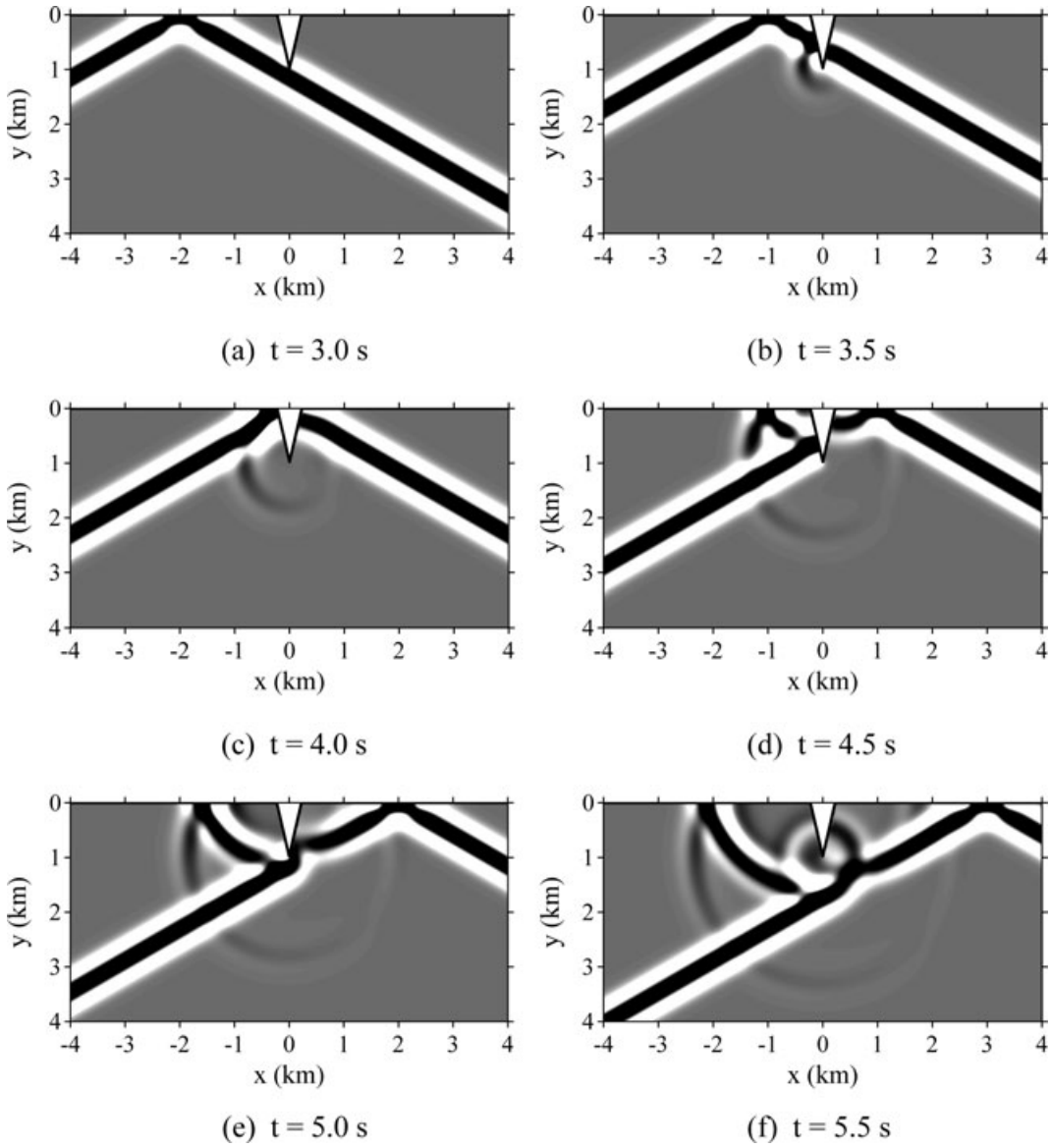

Figure 12. Snapshots for $a/d = 0.25$ and $\alpha = 30^\circ$ at 12 specified times.

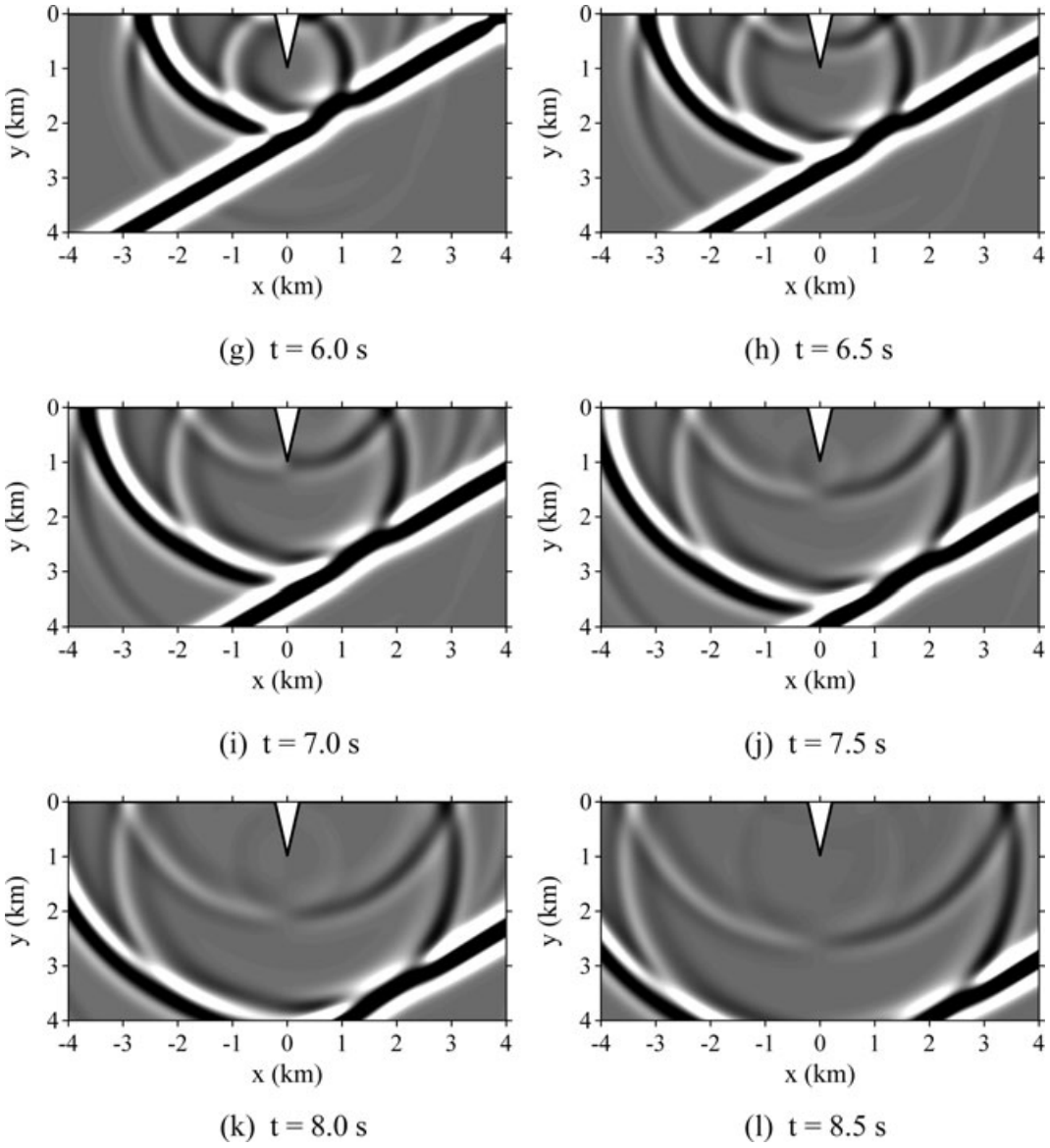

Figure 12. (*Continued*.)

de-amplified due to the destructive interference between the incident and scattered waves from the RUC of the canyon.

As seen at the top of Fig. 11, three wave signals received after the signal of direct wave are labelled, in turn, by arrows $L1$, $L2$ and $L3$. The arrows $L1$ and $L2$ denote, respectively, the reflected wave from the left-hand canyon surface (see Fig. 12d) and the scattered waves from the canyon bottom (see Fig. 12b). The arrow $L3$ denotes the scattered waves originated from the LUC and bottom of the canyon (see Figs 12f–h). Similarly, as observed at the foot of Fig. 11, there are three wave signals received one by one after the signal of direct wave. They are tagged by arrows $R1$, $R2$ and $R3$. The arrows $R1$ and $R2$ denote, respectively, the scattered waves originated from the canyon bottom (see Figs 12f–h) and the RUC of the canyon (see Figs 12d–h). The arrow $R3$ also denotes the scattered waves from the canyon bottom and the RUC of the canyon (see Figs 12f–h). In addition, the amplitudes of scattered waves $R1$ and $R2$ are smaller than that of $R3$.

In Fig. 12, one can perceive how the incident SH pulse reaches the canyon and how a chain of scattered waves propagates. As seen in Fig. 12(a), the incoming pulse and its corresponding reflected pulse from the horizontal ground surface arrive at the position $(-2, 0)$ at $t = 3.0$ s, and the former impinges on the canyon bottom. In Fig. 12(b), the scattered wave (i.e. $L2$ and $R1$ in Fig. 11) radiating from the canyon bottom can be found. In Fig. 12(c), the incident pulse and its reflected pulse reach both upper corners of the canyon. From Fig. 12(d), one can observe that the reflected wave from the horizontal ground surface bumps into the left-hand canyon surface so that a new reflected wave (i.e. $L1$ in Fig. 11) is produced. Furthermore, the scattered wave (i.e. $R2$ in Fig. 11) arises from the RUC of the canyon. Subsequently, at the canyon base (see Fig. 12e), this scattered wave meets two reflected waves from the horizontal ground surface and from the left-hand canyon surface. In Fig. 12(f), a new scattered wave (i.e. $L3$ and $R3$ in Fig. 11) is generated from the canyon base and hits both upper corners of the canyon later (see Fig. 12g). As can be found in Figs 12(b)–(l), the bottom and both upper corners of the canyon behave as new wave sources. Several scattered waves radiated from the canyon bottom are antisymmetric to the y-axis and those shown in Figs 12(i)–(l) are of very small

amplitude (not easily detected in Fig. 11). Besides, the diffraction around the V-shaped canyon can be directly visualized. The characteristic feature of the diffraction is that a part of the reflected wave front from the horizontal ground surface is cut off by the V-shaped canyon and then continuously regenerates itself.

4 CONCLUSION

The scattering problem of SH waves triggered by a deep symmetrical V-shaped canyon has been solved successfully via a novel analytical approach. An ingenious employment of domain decomposition has guaranteed the full encirclement of deep canyons so that the stress singularity condition at the bottom of the canyon could be satisfied automatically. Through making good use of the region-matching technique, the method of images, and Graf's addition formulas, a rigorous series solution has been derived. For the deep V-shaped cases, there has been good consistency between the calculated results of derived series solution and those in the literature. For the limiting cases, the computed results for surface amplitudes and DSIF have agreed well with those from the exact series solution of a single vertical edge crack. These evidences have reinforced the validity and reliability of the whole framework of present formulations. Both steady-state and transient variations in surface ground motions have been evaluated and analysed. Since the series solution to the shallow cases had been derived (see Tsaur & Chang 2008), and that to the deep cases has been proposed herein, the construction of series solutions to the SH-waves scattering problem of a single symmetrical V-shaped canyon has been complete. Indeed, these proposed series solutions not only enrich the records of known geometrical shapes of canyons, but also provide useful benchmark examples for validating other numerical methods. In addition, the adopted solution scheme can be applied to attack the scattering problems of SH waves induced by other surficial concave topography with corners.

ACKNOWLEDGMENTS

We would like to thank the Editor, Prof. Xiaofei Chen for processing our manuscript and his encouragement, and two referees for their comments and suggestions on this work.

REFERENCES

Abramowitz, M. & Stegun, I.A., 1972. *Handbook of Mathematical Functions, with Formulas, Graphs, and Mathematical Tables,* Dover, New York.

Boore, D.M., 1973. The effect of simple topography on seismic waves: implications for the accelerations recorded at Pacoima Dam, San Fernando Valley, California, *Bull. seism. Soc. Am.,* **63,** 1603–1609.

Bouchon, M., 1973. Effect of topography on surface motion, *Bull. seism. Soc. Am.,* **63,** 615–632.

Datta, S.K. & Shah, A.H., 1982. Scattering of SH waves by embedded cavities, *Wave Motion,* **4,** 265–283.

Hirai, H., 1988. Analysis if transient response of SH wave scattering in a half space by the boundary element method, *Eng. Anal.,* **5,** 189–194.

Huang, H.C. & Chiu, H.C., 1995. The effect of canyon topography on strong ground motion at Feitsui damsite: quantitative results, *Earthq. Eng. Struct. Dyn.,* **24,** 977–990.

Kawase, H., 1988. Time-domain response of a semi-circular canyon for incident SV, P and Rayleigh waves calculated by the discrete wavenumber boundary element method, *Bull. seism. Soc. Am.,* **78,** 1415–1437.

Liu, D.K. & Han, F., 1991. Scattering of plane SH wave by cylindrical canyon of arbitrary shapes, *Soil Dyn. Earthq. Eng.,* **10,** 249–255.

Sabina, F.J. & Willis, J.R., 1975. Scattering of SH waves by a rough half-space of arbitrary slope, *Geophys. J. R. astr. Soc.,* **42,** 685–703.

Sánchez-Sesma, F.J. & Rosenblueth, E., 1979. Ground motion at canyons of arbitrary shape under incident SH waves, *Earthq. Eng. Struct. Dyn.,* **7,** 441–450.

Shah, A.H., Wong, K.C. & Datta, S.K., 1982. Diffraction of plane SH waves in a half-space, *Earthq. Eng. Struct. Dyn.,* **10,** 519–528.

Sills, L.B., 1978. Scattering of horizontally-polarized shear waves by surface irregularities, *Geophys. J. R. astr. Soc.,* **54,** 319–348.

Stone, S.F., Ghosh, M.L. & Mal, A.K., 1980. Diffraction of antiplane shear waves by an edge crack, *J. Appl. Mech. ASME,* **47,** 359–362.

Takemiya, H. & Fujiwara, A., 1994. SH-wave scattering and propagation analysis at irregular sites by time domain BEM, *Bull. seism. Soc. Am.,* **84,** 1443–1455.

Tsaur, D.H., 2010. Exact scattering and diffraction of antiplane shear waves by a vertical edge crack, *Geophys. J. Int.,* **181,** 1655–1664.

Tsaur, D.H. & Chang, K.H., 2008. An analytical approach for the scattering of SH waves by a symmetrical V-shaped canyon: shallow case, *Geophys. J. Int.,* **174,** 255–264.

Varadan, V.V., Ma, Y., Varadan, V.K. & Lakhtakia, A., 1991. Scattering of waves by spheres and cylinders, in *Field Representations and Introduction to Scattering,* pp. 211–324, eds Varadan, V.V., Lakhtakia, A. & Varadan, V.K., North-Holland, Amsterdam.

Watson, G.N., 1958. *A Treatise on the Theory of Bessel Functions,* 2nd edn, Cambridge University Press, Cambridge.

Zhang, C. & Zhao, C., 1988. Effects of canyon topography and geological conditions on strong ground motion, *Earthq. Eng. Struct. Dyn.,* **16,** 81–97.

APPENDIX A: EXPRESSIONS OF $I^{C1}_{n,q}(\beta)$, $I^{C2}_{n,q}(\beta)$, $I^{S1}_{n,q}(\beta)$ AND $I^{S2}_{n,q}(\beta)$

In eqs (14) and (15), the functions $I^{C1}_{n,q}(\beta)$ and $I^{C2}_{n,q}(\beta)$ are defined by

$$I^{C1}_{n,q}(\beta)=\begin{cases}2\beta, & n=q=0\\ \beta+\frac{\sin 2q\beta}{2q}, & n=q\\ \frac{\sin[(n-q)\beta]}{n-q}+\frac{\sin[(n+q)\beta]}{n+q}, & n\neq q\end{cases} \tag{A1}$$

$$I^{C2}_{n,q}(\beta)=\begin{cases}2\beta, & n=q=0\\ \beta+\frac{\sin 2q\beta}{2q}, & n\nu=q\\ \frac{\sin[(n\nu-q)\beta]}{n\nu-q}+\frac{\sin[(n\nu+q)\beta]}{n\nu+q}, & n\nu\neq q\end{cases}. \tag{A2}$$

In eqs (16) and (17), the functions $I^{S1}_{n,q}(\beta)$ and $I^{S2}_{n,q}(\beta)$ are defined by

$$I^{S1}_{n,q}(\beta)=\begin{cases}\beta-\frac{\sin 2q\beta}{2q}, & n=q\\ \frac{\sin[(n-q)\beta]}{n-q}-\frac{\sin[(n+q)\beta]}{n+q}, & n\neq q\end{cases} \tag{A3}$$

$$I^{S2}_{n,q}(\beta)=\begin{cases}\beta-\frac{\sin 2q\beta}{2q}, & n\nu=q\\ \frac{\sin[(n\nu-q)\beta]}{n\nu-q}-\frac{\sin[(n\nu+q)\beta]}{n\nu+q}, & n\nu\neq q\end{cases}. \tag{A4}$$